A projection-based level-set approach to enhance conductivity anomaly reconstruction in electrical resistance tomography

M K Ben Hadj Miled[1] **and E L Miller**[2]

[1] Center for Subsurface Sensing and Imaging Systems, Northeastern University, 315 Stearns Hall, Boston, MA 02115-5000, USA
[2] Department of Electrical and Computer Engineering, Tufts University, Halligan Hall, 161 College Ave., Medford MA 02155, USA

E-mail: mkmiled@ece.neu.edu and elmiller@ece.tufts.edu.com

Abstract
In this paper we consider level-set-based methods for anomaly reconstruction for applications involving low-sensitivity data concentrating specifically on the problem of electrical resistance tomography (ERT). Typical descent-based inversion methods suffer from poor reconstruction precision in low-sensitivity regions and typically display quite slow convergence. In this paper, we develop a method for constructing the level-set speed function that is capable of overcoming these problems. In the case of the gradient-descent-based level-set evolution, the speed function is defined in terms of the dot products of residual and sensitivity functions. For Gauss–Newton-type methods, however, the speed function is the solution of the linearized inverse problem at each iteration. Here we propose a projection-based approach where the displacement of the level zero, i.e. estimated anomaly contour, at each point depends on the correlation coefficients between the sensitivity of the data to conductivity perturbations and the residual error. In other words, the proposed velocity field is invariant to the absolute amplitudes of both residual and sensitivity, but rather is a reflection of the angle between these two quantities. We demonstrate that our method is a descent-based reconstruction and we relate the mathematical formulation of the projection-based speed function to that of the gradient-descent method and the Gauss–Newton-type approach. The comparison suggests that the proposed technique can be seen as a diagonal approximation of the Gauss–Newton formulation. Using a quasi-linear source-type formulation of the forward problem, we describe an efficient implementation of the projection-based approach for finite-domain imaging problems. The proposed algorithm is simulated with numerical 2D and 3D data and its performance and efficiency are compared to those of the gradient-descent method.

(Some figures in this article are in colour only in the electronic version)

1. Introduction

The objective of electrical resistance tomography (ERT) and its close counterpart electrical impedance tomography (EIT) is to reconstruct the electrical properties within a medium of interest based on measured boundary electric currents and electric potentials. The idea dates back to the Schlumberger and Wenner electrode arrays used as resistivity probing systems to detect earth subsurface structures [1]. Potential applications now range from medical imaging [2–9] and non-destructive evaluation [10–13] to geophysical exploration [14, 15] and environmental monitoring [16–19]. The conductivity reconstruction problem, based on complete boundary electric signals, was first formulated by Caldéron [20] and the solution was shown to be unique [21–24] under a variety of assumptions. The inverse problem is known to be highly ill-posed [25, 27]. The ill-posedness is mainly due to the low dimension of measured data vectors compared to the usually much larger number of unknown conductivity grid points, in a discretized medium, and the very sensitivity of observation data to conductivity variations at regions far away from sensor electrodes. The scope of this paper is a reconstruction approach for anomalies (i.e. well-defined regions that are, in a sense, 'different' from some nominal background) that is less prone to low-sensitivity effects.

In the literature, several iterative and noniterative reconstruction methods have been proposed for addressing the conductivity reconstruction problem (see the topical reviews [25–27]). Noniterative techniques include the backprojection algorithm [28–30], layer stripping methods [33–35] and the $\bar{\partial}$ method [36, 37]. Another method is the NOSER algorithm [9, 31, 32] which is a single Gauss–Newton step regularized with a diagonal approximation of the Hessian. The work by Brühl and Hanke [38, 39] characterizes conductivity inclusions in terms of point-dipole sources embedded in a homogeneous background medium and having the same support as the anomalies they characterize. The reconstruction in this case is a localization of such sources using a MUSIC-type approach.

Iterative full pixel/voxel reconstruction of the conductivity is usually formulated as a constrained [40–42] or an unconstrained [19, 43–45] least-squares optimization problem. Gradient-based algorithms are then used to minimize a cost function incorporating data misfit and prior information as a regularization term. In particular, the conjugate gradient approach has been widely used. However, recently there has been considerable work concerning alternative Newton-type methods for general large-scale distributed parameter estimation designed to achieve improved computational efficiency and faster convergence [46–50]. Given an *a priori* model of the conductivity, the regularization is then achieved by penalizing a distance between the estimate and *a priori* models [19, 43, 45]. Beyond this penalty, the methods in [40–42] restrict the conductivity update, at each iteration, to a pre-defined subspace. Another regularization approach is to enforce some smoothing behavior on the solution [44]. In the variationally constrained approach [53] the set of admissible solutions is constrained by both Dirichlet and Thompson feasibility conditions whereas inversion with basis constraints [54] restricts conductivity distribution to a function subspace defined by a set of basis functions. Other techniques include statistical inversion [55, 56] and multigrid methods [57–59] where reconstruction is performed at different resolutions starting with the coarse one where the inverse problem is less ill-posed.

In recent years there has been significant interest in shape-based reconstruction of anomalies via the level-set approach [60–65]. The level-set method is believed to regularize the ill-posed problem in 'a topological fashion' [61] with the flexibility to reconstruct an unknown number of disjoint regions with no increase in algorithmic complexity. In most of the proposed level-set formulations, the evolution of the anomaly interface is driven by a gradient-descent velocity field defined in terms of the inner product of the forward and adjoint

fields [64, 66, 67]. A regularization term penalizing either the length of the estimated interface or the variation in the conductivity map is usually applied to enforce a smooth boundary of the estimated anomaly. The common observation about the gradient-descent evolution is the slow convergence. In [68], we suggested a speed equalization technique where steepest-descent velocity is scaled in such a way as to shrink its range and relatively enhance the interface evolution at low-sensitivity regions. Other level-set methods apply a Gauss–Newton-type [69, 70] or a Levenberg–Marquardt [71] velocity field. These approaches are usually associated with a computational burden as they require, at each iteration, the evaluation of the Jacobian of the forward model and the inversion of a relatively large matrix. However, a narrow-band implementation of the level set method can reduce the computational cost significantly [70]. In addition, efficient implementations of Gauss–Newton-type methods are described in [48]. Recent work on level-set methods for large-scale distributed parameter estimation [72] compares Gauss–Newton and Levenberg–Marquardt methods. Several variants of the total variation approach are proposed for regularizing the level-set function by forcing it to be as close as possible to a signed distance function. For more on level sets, the reader is referred to the topical review [73].

In this paper we propose a speed function that, empirically, converges much more rapidly than gradient descent without the computational burden of a Gauss–Newton-type approach. Considering a variational formulation, the gradient-descent speed function can be described in terms of the sum, over all data sets, of the dot products of sensitivity and residual error functions evaluated at receiver electrodes. This results in a very slow evolution of the interface in low-sensitivity regions of the domain, e.g., in areas far from sources and detectors or deep within concavities of a conductivity anomaly. We introduce a new speed function defined as the summation of the corresponding correlation coefficients, instead of dot products, between sensitivity functions and residuals. This projection-based level-set method is shown to be a descent approach. We clarify the intuition behind the proposed inversion technique by relating it to the gradient-descent and Gauss–Newton methods. Using a source-type description we outline a numerical approximation to transform the inverse problem into multi-source inversion in an unbounded medium given dense sampling of boundary data. Such a transformation makes it possible to compute sensitivity functions analytically and therefore saves us an excess of forward or adjoint solves. Using simulation data, we compare the results of the projection-based approach to those of the gradient-descent method. In our comparison we focus mainly on relatively complex anomaly structures characterized either with deep concavities, usually associated with low sensitivity, or multiple objects. Relative to the gradient-descent approach, our results show that the projection-based level-set method has a much faster convergence to a more accurate reconstruction. The proposed approach is also stable, even with an initial guess that is far from the actual anomaly, and robust to additive noise.

The paper is organized as follows. In the next section, we formulate the forward and inverse problems and we introduce the quasi-linear source-type formulation. In section 3 we introduce the projection-based level-set approach and we relate it to the gradient-descent and Gauss–Newton methods. We also lay out a very efficient implementation of the proposed algorithm. Finally, simulation results are presented and discussed and the paper is concluded.

2. Problem formulation

2.1. Forward model

Consider a medium $\mathcal{D} \in \mathbb{R}^d, d = 2$ or 3, with a boundary $\partial \mathcal{D}$. We denote by $\sigma(r) > 0$ the conductivity distribution inside $\mathcal{D}$. Throughout this paper, we consider piecewise constant

conductivity distributions of the form

$$\sigma(r) = \begin{cases} \sigma_b + \sigma_a & \text{for } r \in \Omega \\ \sigma_b & \text{for } r \in \mathcal{D} \backslash \Omega \end{cases}, \tag{1}$$

where σ_b is the background conductivity value. The domain Ω represents the inhomogeneity region and σ_a is the contrast in conductivity between anomaly and background regions. The sub-domain Ω is assumed to be the union of a finite number of disjoint, but simply connected, compact subsets of $\mathcal{D}$. We define Γ as the interface separating anomalies from background, i.e. $\Gamma = \partial \Omega$.

Given a current density f across $\partial \mathcal{D}$, the resulting potential function u is defined by the Neumann boundary value problem

$$\nabla \cdot (\sigma \nabla u) = 0, \qquad \sigma \frac{\partial u}{\partial n} = f, \tag{2}$$

where n is the outward unit normal on $\partial \mathcal{D}$. The current density function f obeys the conservation of charge relation

$$\oint_{\partial \mathcal{D}} f(r) \, ds(r) = 0. \tag{3}$$

The forward problem defined by (2) and (3) has a unique weak solution u_σ up to an additive constant. In this paper we consider solutions with a zero-mean boundary potential, i.e. $\oint_{\partial \mathcal{D}} u_\sigma(r) \, ds(r) = 0$.

In the boundary value problem described in (2), the electric potential is a nonlinear function of σ. However, in the case of a background medium with constant conductivity, i.e. $\sigma(r) = \sigma_b$ for every $r \in \mathcal{D}$, the forward problem is linear in terms of background resistivity $\rho_b = \sigma_b^{-1}$:

$$\sigma_b \Delta u_b = 0, \qquad \sigma_b \frac{\partial u_b}{\partial n} = f. \tag{4}$$

In other words, the nonlinearity is introduced by conductivity inhomogeneity. The effect of the anomalies on the electric potential is defined by the scattered potential $u_s = u - u_b$. In appendix A we show that u_s can be described as the solution of a quasi-linear[3]'1 homogeneous boundary value problem, i.e.

$$-\sigma_b \Delta u_s = \sigma_a (\nu \cdot \nabla u), \qquad \sigma_b \frac{\partial u_s}{\partial n} = 0, \tag{5}$$

where ν is the outward unit normal on Γ. The term $\sigma_a(\nu \cdot \nabla u)$ represents a continuum of secondary sources distributed on the interface Γ. In [38, 39] a different source-type characterization based on point-dipole sources spanning the inside area (or volume) of conductivity anomalies is described. The secondary sources in (5) are single-pole sources with amplitudes that are linearly dependent on the conductivity contrast and the component of the total electric field that is in the normal direction of Γ. Note that u in (5) represents the total electric potential, which is the solution of the forward problem (2). Figure 1 illustrates the distribution of secondary sources for a rectangular conductivity anomaly under the effect of horizontal and vertical cross-drive current flows. Numerically, the scattered potential is computed first and then $\sigma_b \Delta u_s$ is evaluated to find the distribution of equivalent sources as described by (5). The results clearly illustrate the facts that the support of secondary sources is restricted to Γ and that their amplitudes depend on the electric field direction with respect to ν, i.e. the unit normal on Γ.

---

[3] Quasi-linearity means that the nonlinearity here is not associated with the higher-order term in the differential equation.
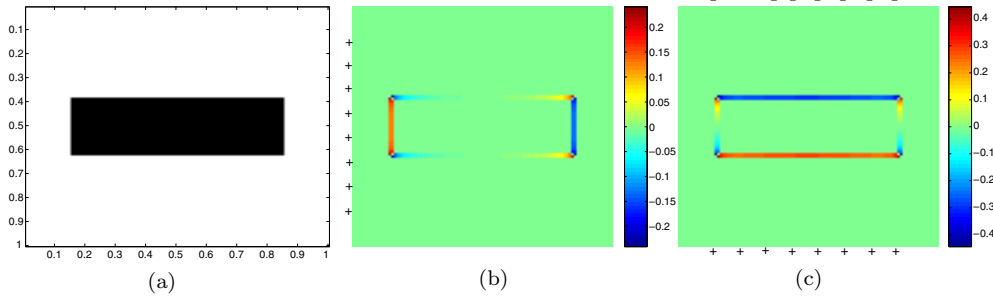
Figure 1. The distributional behavior of equivalent secondary sources, for a rectangular anomaly, under the effect of horizontal and vertical cross-drive current flow. The + and − signs indicate the locations of, respectively, positive and negative primary current sources at the boundary. (a) Conductivity map, (b) secondary sources under horizontal current flow and (c) secondary sources under vertical current flow.

The summation of (4) and (5) leads to a source-type quasi-linear formulation of the forward problem, i.e.

$$\sigma_b \Delta u = \sigma_a (v \cdot \nabla u), \qquad \sigma_b \frac{\partial u}{\partial n} = f. \tag{6}$$

In this source-type description, the information about the anomaly shape and location is embedded in the secondary source term $\sigma_a(v \cdot \nabla u)$. The analytical solution of (6) can be described, for each point $r \in \mathcal{D}$, by the source-type integral equation

$$u(r) = \rho_b \oint_\Gamma c(q)g(q,r)\,\mathrm{d}s(q) + \oint_{\partial \mathcal{D}} \left(u(q) \frac{\partial g(q,r)}{\partial n_q} - \rho_b f(q) g(q,r) \right) \mathrm{d}s(q), \tag{7}$$

where $c(q) = \sigma_a(v(q) \cdot \nabla u(q))$ is the secondary sources term and $g(q,r)$ is the Green's function of the Laplacian operator. The first term on the right-hand side of (7) represents the electric potential generated by the secondary sources if they were embedded in an unbounded homogeneous medium. The second term however describes the contribution of the medium boundary, i.e. $\partial \mathcal{D}$, to the total electric potential. In sub-section 3.2 we make use of (7) to provide an efficient numerical implementation, specifically for problems involving bounded domains, of our correlation-based level-set speed function.

2.2. Inverse problem

The goal in this paper is to identify conductivity anomalies based on observations of the static boundary potential $u|_{\partial \mathcal{D}}$. We assume that both background and anomaly conductivity values σ_b and σ_a are known *a priori* and the inverse problem is to reconstruct Γ. We consider L experiments each with current density f_l and boundary observation z_l, $l = 1, \ldots, L$. The inverse problem can then be described as a minimization of the cost function

$$\mathcal{J}(\Gamma) = \frac{1}{2} \sum_{l=1}^L \oint_{\partial \mathcal{D}} |u_l(q) - z_l(q)|^2 \,\mathrm{d}s(q) + \gamma \oint_\Gamma \mathrm{d}s, \tag{8}$$

where the functions u_l represent the computed potential, using a numerical forward model. The second integral is a penalty on the length of Γ and γ is a small positive real number [64].

The regularization term in (8) penalizes anomalies' perimeter and therefore enforces a smooth interface. In this paper, the focus is mainly on a new descent approach minimizing

the residual mismatch error with respect to observation data. The proposed approach can also be implemented with other regularization techniques such as total variation [66, 67] or its variants [72]. Such implementations are beyond the scope of this paper.

3. Inversion

3.1. Level sets

For the reconstruction of Γ the level set approach, which was first introduced by Osher and Sethian [74], provides a flexible and efficient framework based on topological evolution of interfaces. Considering the level-set function $\phi(r, t), t \geqslant 0, r \in \mathbb{R}^d$, estimates of Ω, Γ and $\sigma(r)$ through time are then defined as

$$\Gamma_t = \{r \in \mathcal{D} : \phi(r, t) = 0\}, \tag{9}$$

$$\Omega_t = \{r \in \mathcal{D} : \phi(r, t) < 0\}, \tag{10}$$

$$\sigma_t(r) = \begin{cases} \sigma_b + \sigma_a & \text{for} \quad \phi(r, t) < 0 \\ \sigma_b & \text{for} \quad \phi(r, t) > 0 \end{cases}. \tag{11}$$

The level-set evolution is defined by the Hamilton–Jacobi system [76]

$$\frac{\partial \phi}{\partial t} + V(r, t) \cdot \nabla \phi = 0, \qquad \phi(r, 0) = \phi_0(r), \tag{12}$$

where $V(r, t)$ is the velocity field at time t and $\phi_0(r)$ is the initial level-set function. The velocity field enforces an evolution in the normal direction of Γ_t, i.e. $V(r, t) = v(r, t)\nu$ where v is a scalar speed function and $\nu = \frac{\nabla \phi}{|\nabla \phi|}$ is the unit normal on Γ_t.

Consider a 2 D grid $\{(x_i, y_j)\}_{i=1,\ldots,n_x, j=1,\ldots,n_y}$ where n_x and n_y are the numbers of grids in the x and y directions, respectively. The numerical implementation of the first-order hyperbolic differential equation (12) can be described as

$$\phi(x_i, y_j, t_{k+1}) = \phi(x_i, y_j, t_k) + v(x_i, y_j, t_k)|\nabla \phi(x_i, y_j, t_k)|\tau_k, \tag{13}$$

where $0 = t_0 < t_1 < \cdots < t_m = T$ is the time grid and τ_k is the time step at each iteration. Building on previous work [65, 75], the level set implementation used in this paper applies the CFL condition to maintain a stable Hamilton–Jacobi solver , i.e.

$$\tau_k \max_{i,j} |v(x_i, y_j, t_k)| < h \qquad \forall k \in [0, \ldots, m-1] \tag{14}$$

where h is the typical spatial grid size. The stability constraint applies similarly to a 3D grid and is meant to prevent the interface from moving by more than a pixel/voxel length at any iteration [76]. In our implementation the time step τ_k is computed as

$$\tau_k = \eta \frac{h}{\max_{i,j} |v(x_i, y_j, t_k)|}, \tag{15}$$

where $0 < \eta < 1$ and at each iteration the value of η is defined by a line search algorithm.

3.2. Projection-based velocity field

A key component in any inversion method is the sensitivity of the data to variations in the unknown to be reconstructed, in our case $\sigma(r)$. The sensitivity functions $u'_{l,r}$, which describe the change in potential functions u_l due to conductivity perturbation at a location r, come into play in the functional derivative of the cost function. Assuming that $\gamma = 0$ for a moment, from (8), it is easy to show that the functional derivative of the cost function is

$$\frac{\mathrm{d}\mathcal{J}}{\mathrm{d}\sigma} = \sum_{l=1}^{L} \oint_{\partial\mathcal{D}} u'_{l,r}(q)(u_l(q) - z_l(q)) \, \mathrm{d}s(q) \tag{16}$$

$$= \sum_{l=1}^{L} (u'_{l,r}, u_l - z_l)_{\partial\mathcal{D}}, \tag{17}$$

where $(\cdot, \cdot)_{\partial\mathcal{D}}$ represents the dot product of two functions evaluated on $\partial\mathcal{D}$. It is important to note at this point that the evaluation of $u'_{l,r}$ on $\partial\mathcal{D}$ requires solving the boundary value problem (B.2) for each experiment–location pair (l, r). By applying the chain rule, as in [67], the shape derivative of the cost function with respect to variations in the level-set function φ is

$$\frac{\mathrm{d}\mathcal{J}}{\mathrm{d}\varphi} = \frac{\mathrm{d}\mathcal{J}}{\mathrm{d}\sigma}\frac{\mathrm{d}\sigma}{\mathrm{d}\varphi}$$

$$= \oint_{\Gamma_t} \left(\sum_{l=1}^{L} (u'_{l,r}, u_l - z_l)_{\partial\mathcal{D}} \right) \sigma_a v(r, t) \, \mathrm{d}s(r). \tag{18}$$

According to equation (18), the level set formulation provides considerable flexibility in defining the speed function as long as the latter guarantees a non-increasing cost, that is, $\frac{\mathrm{d}\mathcal{J}}{\mathrm{d}\varphi} \leqslant 0$.

One natural choice, for the speed function, is the gradient-descent approach [60, 64, 65] with

$$v_{gd}(r, t) = -\mathrm{sign}(\sigma_a) \left(\sum_{l=1}^{L} (u'_{l,r}, u_l - z_l)_{\partial\mathcal{D}} \right). \tag{19}$$

The main term in the gradient descent speed function is the summation, over all experiments, of the dot products of boundary residual and sensitivity functions, i.e. $u_l - z_l$ and $u'_{l,r}$, respectively. These dot products can be described as

$$(u'_{l,r}, u_l - z_l)_{\partial\mathcal{D}} = |u_{l,r}||u'_l - z_l| \cos(\theta_{l,r}), \tag{20}$$

where $|u_l - z_l|$ and $|u_{l,r}|$ represent the $\mathcal{L}_2$-norms of the residual and sensitivity functions, respectively, and $\cos(\theta_{l,r})$ describes the cosine of the angle, or correlation coefficient, between the same functions.

In our approach we propose the use of correlation coefficients, instead of dot products, as a metric for the projection of sensitivity functions onto residual signals. In other words, we consider the speed function

$$v_p(r, t) = -\mathrm{sign}(\sigma_a) \sum_{l=1}^{L} \frac{(u'_{l,r}, u_l - z_l)_{\partial\mathcal{D}}}{|u'_{l,r}||u_l - z_l|} \tag{21}$$

$$= -\mathrm{sign}(\sigma_a) \sum_{l=1}^{L} \cos(\theta_{l,r}). \tag{22}$$

As described in (19), the projection-based speed function is very much dependent on the similarity between normalized sensitivity and residual functions but invariant to the sensitivity and residual norms. This invariance makes the approach less prone to spatial variation in sensitivity amplitudes and changes in residual error energy with respect to distinct data sets, i.e. experiments.

The projection-based method, described in (21), is a descent approach. Substituting equations (20) and (21) into (18), the latter can then be re-written as

$$\frac{\mathrm{d}\mathcal{J}}{\mathrm{d}\varphi} = |\sigma_a| \oint_{\Gamma_t} \left(\sum_{l=1}^{L} \sum_{m=1}^{L} |u'_{l,r}||u_l - z_l| \cos(\theta_{l,r}) \cos(\theta_{m,r}) \right) \mathrm{d}s(r) \tag{23}$$

$$= |\sigma_a| \oint_{\Gamma_t} (\mathbf{a}^T \mathbf{B} \mathbf{a}) \, \mathrm{d}s(r), \tag{24}$$

where $\mathbf{a}^T = [\cos(\theta_{L,r}) \cdots \cos(\theta_{1,r})]$ and $\mathbf{B}$ is the semi-definite matrix, of rank 1, defined as

$$\mathbf{B} = \begin{pmatrix} |u'_{1,r}||u_1 - z_1| & \cdots & |u'_{L,r}||u_L - z_L| \\ \vdots & \vdots & \vdots \\ |u'_{1,r}||u_1 - z_1| & \cdots & |u'_{L,r}||u_L - z_L| \end{pmatrix}. \tag{25}$$

The integrand in (24) is non-negative and so is the derivative of the cost function $\frac{\mathrm{d}\mathcal{J}}{\mathrm{d}\varphi}$.

3.3. Projection-based approach versus classical level-set speed functions

In this subsection we relate the proposed projection-based speed function to gradient-descent and Gauss–Newton-type velocity functions. The goal is to highlight the relationship between our approach and these methods and to provide an intuitive explanation why the proposed projection-based approach is expected to converge faster compared to gradient-descent level-set evolution.

3.3.1. Projection-based approach and the gradient-descent method. In the literature, e.g. [64, 67], the shape derivative in (18) is usually described in terms of the adjoint potentials defined as

$$\nabla \cdot (\sigma \nabla w_l) = 0, \qquad \sigma \frac{\partial w_l}{\partial n} = u_l - z_l. \tag{26}$$

Using the fact that $(u'_{l,r}, u_l - z_l)_{\partial \mathcal{D}} = \nabla u_l(r) \cdot \nabla w_l(r)$ (see appendix B for a detailed derivation), the gradient-descent speed function is expressed as

$$v_{gd}(r, t) = -\mathrm{sign}(\sigma_a) \left(\sum_{l=1}^{L} \nabla u_l(r) \cdot \nabla w_l(r) \right). \tag{27}$$

Computationally, the expression in (27) involves solving one adjoint problem (26) per source/data set, whereas the variational formulation (19) requires, upon discretization of the inverse problem, solving the boundary value problem (B.2) for each experiment–location pair (l, r) in order to evaluate $u'_{l,r}$. Considering the adjoint formulation (27), the projection-based speed function can also be described as

$$v_p(r, t) = -\mathrm{sign}(\sigma_a) \left(\sum_{l=1}^{L} \frac{\nabla u_l(r) \cdot \nabla \bar{w}_l(r)}{|u'_{l,r}|} \right) \tag{28}$$

where $\bar{w}_l$ is the solution of the adjoint problem (26) with boundary current flow equal to $\frac{u_l - z_l}{|u_l - z_l|}$ instead of $u_l - z_l$.

The variational formulations (19) and (21) provide a better distinction, in our view, of our approach with respect to the steepest descent. The correlation coefficient is basically a normalized measure of the similarity between the residual and sensitivity functions.
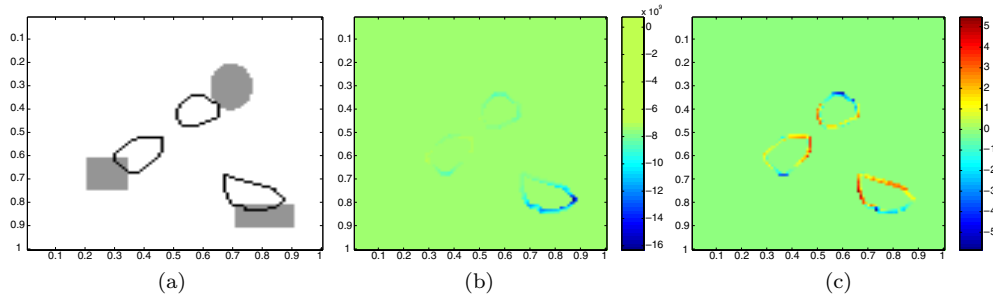
Figure 2. Illustration of the difference between gradient-descent and projection-based speed. (a) shows the actual conductivity map (in gray) and the boundary Γ_t (in black) of a hypothetical estimate of the conductivity distribution, (b) and (c) illustrate the v_{gd} gradient-descent and the projection-based v_p speeds, respectively, evaluated at Γ_t. While projection-based speed is consistent with mismatch between actual and estimate conductivities, the gradient-descent speed function has significant values only in high-sensitivity regions, i.e. at portions of Γ_t that are closest to $\partial\mathcal{D}$. (a) Resistivity maps, (b) gradient-descent speed and (c) projection-based speed.

Alternatively, from (19) the gradient descent approach provides an un-normalized descent direction. More specifically, the presence of $|u_l - z_l|$ indicates that large residuals are a major influence of the gradient-descent level-set evolution. Similarly, $|u'_{l,r}|$ provides greater weight to regions where there is high physical sensitivity. Though, perhaps, one may think that these are precisely the drivers one would want for evolving the level-set function, in practice they tend to dominate the evolution to the extent that (1) information content in data sets with smaller residual is effectively ignored and (2) the evolution of the level-set function in regions of low physical sensitivity is greatly slowed.

Figure 2 illustrates the difference between the two speed functions, for a given conductivity map with three anomalies (an ellipse, a square and a rectangle), at a hypothetical estimate of the conductivity distribution with three inhomogeneity regions each of which overlaps partially with one of the actual anomalies. The speed functions are evaluated over a thin narrow-band defined in the neighborhood of the boundary of the estimated anomalies. Positive values of the speed function indicate that the estimated anomaly should shrink at the corresponding portion of the boundary, i.e. velocity vector pointing inside the anomaly, whereas negative values indicate that the boundary should move in the outward normal direction leading to an expansion of the anomaly. As we see from these figures, the projection-based speed function clearly pushes the estimated anomalies to expand towards the actual ones and shrink at the center of the medium where most of the mismatch, between the actual and estimate conductivities, happens to be. The gradient-descent speed function, however, is significant only on portions of the boundary Γ that are closest to sensor electrodes. In addition, a mismatch between actual and estimated conductivity maps that is close to sensor electrodes has a more significant effect on the residual error than a mismatch that is deep inside the medium. This fact makes the gradient-descent method much slower than the projection-based approach in converging to the actual solution and in some circumstances it might even fail to converge. Later in this paper, the performances of these two methods are compared in more detail.

3.3.2. Projection-based approach and the Gauss–Newton method. The new speed function can be mathematically related to the Gauss–Newton formulation. For the sake of simplicity we consider a configuration with a single source, i.e. single experiment, and therefore omit the subscript l used earlier in the paper to indicate the data set index. We also use a discrete

formulation of the speed functions. Such a representation implies no loss of generality but rather provides a better description for the purpose of showing the link between our approach and the Gauss–Newton method.

Let the vector $\underline{v}_{GN}$ represent a discretized Gauss–Newton speed function evaluated at some estimate Ω_t of the conductivity map. Gauss–Newton-type methods solve the linear problem

$$\mathbf{J}\underline{v}_{GN} = \underline{u} - \underline{z} \tag{29}$$

at each iteration in an iterative reconstruction, where the matrix $\mathbf{J}$ is the Jacobian of the forward model. The Gauss–Newton speed vector can then be expressed as

$$\underline{v}_{GN} = (\mathbf{J}^T\mathbf{J})^{-1}\mathbf{J}^T(\underline{u} - \underline{z}). \tag{30}$$

In the Levenberg–Marquardt formulation the inversion of $\mathbf{J}^T\mathbf{J}$ is regularized with an additional term $\beta\mathbf{R}$, where $\mathbf{R}$ is a positive definite matrix and β is a parameter that is dynamically adjusted [70–72]. The linearized problem (29) implies that in a Gauss–Newton-type approach, one is looking for a linear combination of sensitivity vectors that would best reconstruct the residual error; however, in the proposed projection-based method we seek sensitivity vectors that correlate best with the residual signal, i.e.

$$\underline{v}_p = \frac{1}{|\underline{u} - \underline{z}|}\mathbf{P}^T(\underline{u} - \underline{z}), \tag{31}$$

where $\mathbf{P}$ is the projection matrix whose rows are equal to the normalized sensitivity vectors, i.e. $\mathbf{P} = \left[\frac{\underline{u}'_{1,1}}{|\underline{u}'_{1,1}|} \cdots \frac{\underline{u}'_{n_x,n_y}}{|\underline{u}'_{n_x,n_y}|}\right]^T$, and $\underline{u}'_{i,j}$ is the sensitivity vector for a perturbation at grid point (x_i, y_j).

Considering the fact that the discretized gradient descent speed $\underline{v}_{gd}$ is equal to $\mathbf{J}^T(\underline{u} - \underline{z})$ [60], both Gauss–Newton-type and projection-based speed vectors can also be considered as scaled versions of $\underline{v}_{gd}$. According to (30), $\underline{v}_{GN}$ can be expressed as

$$\underline{v}_{GN} = (\mathbf{J}^T\mathbf{J})^{-1}\underline{v}_{gd}. \tag{32}$$

Defining $\mathbf{G}$ as the diagonal matrix with entries equal to $|\underline{u}'_{i,j}|$, the projection-based speed vector can be written as

$$\underline{v}_p = \frac{1}{|\underline{u} - \underline{z}|}\mathbf{G}^{-1}\underline{v}_{gd}. \tag{33}$$

Recalling the form of the Jacobian as $\mathbf{J} = [\underline{u}'_{1,1} \cdots \underline{u}'_{n_x,n_y}]^T$, then

$$\mathbf{G} = \sqrt{\text{diag}(\mathbf{J}^T\mathbf{J})}. \tag{34}$$

In other words $\mathbf{G}$ is basically a diagonal approximation of $\mathbf{J}^T\mathbf{J}$.

3.3.3. An efficient implementation of the projection-based approach. As described in (21), the evaluation of the projection-based speed function at each iteration involves the computation of sensitivity functions $u'_{l,r}$. In other words, one would solve the boundary value problem (B.2) for each location–experiment pair (r, l). An efficient narrow-band implementation of the level set approach in a discretized medium would require L forward solves, to compute estimates of measured potential, and $L \times M_k$ solves of (B.2) per iteration, where M_k is the number of grid points within the narrow band at the kth iteration. We note that Gauss–Newton methods that construct the Jacobian would require the same number of problem solves [69], adding to that the inversion of the Hessian approximation matrix. However, the gradient-descent approach requires only L forward and L adjoint solves per iteration [43] and efficient implementations

of Gauss–Newton methods perform L forward and $2L$ adjoint solves as well as large matrix inversion [48, 72].

Given the normalization by sensitivity vectors' norms in (21), the projection-based method requires the computation of these sensitivity vectors at least for each pixel/voxel on Γ for every experiment per iteration. This computational burden can be overcome through judicious use of (7). Rewrite the analytical solution of the electric potential, for a piecewise constant medium, as

$$u_l(r) = \rho_b \oint_\Gamma c_l(q)g(q,r)\,\mathrm{d}s(q) + \mathcal{B}(u_l, f_l), \tag{35}$$

where $\mathcal{B}(u_l, f_l)$ is the contribution of the medium boundary $\partial\mathcal{D}$ to the electric potential, i.e.

$$\mathcal{B}(u_l, f_l) = \oint_{\partial\mathcal{D}} \left(u(q)\frac{\partial g(q,r)}{\partial n_q} - \rho_b f(q)g(q,r) \right) \mathrm{d}s(q). \tag{36}$$

Note that the measured electric potential z_l can also be written as

$$z_l(r) = \rho_b \oint_{\Gamma_z} c_{z,l}(q)g(q,r)\,\mathrm{d}s(q) + \mathcal{B}(z_l, f_l), \tag{37}$$

where Γ_z and $c_{z,l}$ represent, respectively, the anomaly boundary and secondary sources corresponding to the measured data. Defining $\tilde{u}_l = u_l - \mathcal{B}(u_l, f_l)$ and $\tilde{z}_l = z_l - \mathcal{B}(z_l, f_l)$, in the projection-based inversion we propose minimizing

$$\tilde{\mathcal{J}} = \frac{1}{2}\sum_{l=1}^{L} \oint_{\partial\mathcal{D}} |\tilde{u}_l - \tilde{z}_l|^2 \,\mathrm{d}s(q) + \gamma \oint_\Gamma \mathrm{d}s \tag{38}$$

instead of $\mathcal{J}$. This modification implicitly implies that the inverse problem is transformed to an identification of the secondary sources as if they were embedded in a homogeneous background medium. Note that the modified inverse problem (38) is a minimization of

$$\tilde{\mathcal{J}} = \frac{\rho_b^2}{2}\sum_{l=1}^{L} \oint_{\partial\mathcal{D}} \left| \oint_\Gamma c_l(q)g(q,r)\,\mathrm{d}s(q) - \tilde{z}_l \right|^2 \mathrm{d}s(r) + \gamma \oint_\Gamma \mathrm{d}s. \tag{39}$$

Sensitivity functions associated with data residual error in (39) can be expressed in terms of Green's functions. The derivations confirming this claim are provided in appendix C where the functions $u'_{l,r}$ are shown to be linearly proportional to $\nabla g(q,r) \cdot v(q)$, where the Green's function $g(q,r)$ for the homogeneous infinite-medium is known analytically. The next step then is the computation of the boundary terms $\mathcal{B}(u_l, f_l)$ and $\mathcal{B}(z_l, f_l)$. Given the assumption that both u_l and z_l are known on the boundary $\partial\mathcal{D}$, the main computational challenge comes with the fact that the boundary-term integral is singular for a point $r \in \partial\mathcal{D}$. In order to avoid singularity, we propose the approximation where the integral is rather evaluated for a point $r' \in \mathcal{D}$ that is a neighbor point of r but not on $\partial\mathcal{D}$. This approximation is not necessarily the most accurate; however, it is good enough not to degrade the reconstruction performance, at least according to our simulation results.

Considering the definitions of $\tilde{u}_l$ and $\tilde{z}_l$ stated above, the corresponding projection-based speed function can then be described as

$$v_p(r, t) = -\mathrm{sign}(\sigma_a) \sum_{l=1}^{L} \frac{(\nabla g \cdot v, \tilde{u}_l - \tilde{z}_l)_{\partial\mathcal{D}}}{|\nabla g \cdot v||\tilde{u}_l - \tilde{z}_l|_{\partial\mathcal{D}}}. \tag{40}$$

Note that sensitivity can be analytically approximated with $c_l \nabla g \cdot v$, as described in (C.6); however, in (40) use the term $\nabla g \cdot v$ instead and omit the unknown amplitudes of secondary sources c_l. This does not affect the final result of the speed functions because the correlation
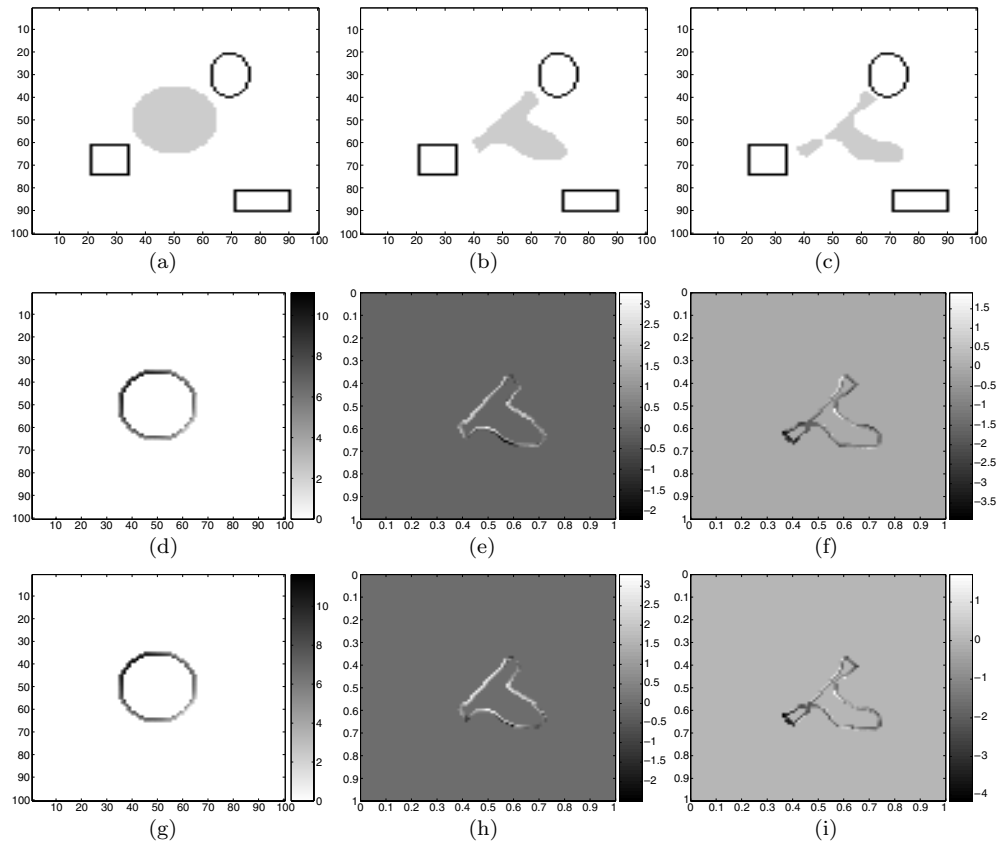
Figure 3. For a conductivity distribution with three disjoint anomalies, the projection-based speed function is evaluated at three distinct conductivity estimates without approximation (second row) and with approximation (third row). The first row shows the boundary of the true conductivity distribution (black lines) and the conductivity estimates (gray regions). (a) Conductivity estimate 1, (b) conductivity estimate 2, (c) conductivity estimate 3, (d) speed function using (21) for estimate 1, (e) speed function using (21) for estimate 2, (f) speed function using (21) for estimate 3, (g) speed function using (40) for estimate 1, (h) speed function using (40) for estimate 2 and (i) speed function using (40) for estimate 3.

coefficients are independent of the magnitudes of sensitivity functions and residual error. In figure 3 we consider three distinct estimates for a conductivity distribution with three disjoint anomalies. For each conductivity estimate the projection-based speed function is evaluated without any approximation, i.e. as in equation (21), and displayed in the second row of the figure. The last row illustrates the speed functions computed using equation (40). Comparing the results in both rows, one can conclude a very similar behavior of the velocity function in both cases. Specifically, along most of the boundary of a conductivity estimate the speed values, computed both ways, have identical signs and a similar distribution of the velocity magnitudes. Therefore, equation (40) results a significant reduction in computational complexity, compared to equation (21), without significant distortion of the behavior of the speed function. In section 4 further simulation results, using the implementation described in this sub-section, are provided to illustrate the efficiency of the projection-based level set approach in reconstructing conductivity anomalies.

For the sake of clarity we emphasize that the method described in this subsection is only applied to the 2D medium projection-based approach. In other words, considering a non-zero γ, the projection-based speed function used in the rest of the paper, for a 2D medium, is defined as

$$v_p(r, t) = -\text{sign}(\sigma_a) \sum_{l=1}^{L} \frac{(\nabla g \cdot \nu, \tilde{u}_l - \tilde{z}_l)_{\partial \mathcal{D}}}{|\nabla g \cdot \nu||\tilde{u}_l - \tilde{z}_l|_{\partial \mathcal{D}}} + \gamma \kappa. \tag{41}$$

where κ is the mean curvature. The gradient-descent speed function, however, is defined as

$$v_{gd}(r, t) = -\text{sign}(\sigma_a) \left(\sum_{l=1}^{L} \nabla u_l(r) \cdot \nabla w_l(r) \right) + \gamma \kappa, \tag{42}$$

where u_l and w_l are the forward and adjoint potentials, respectively, in the lth experiment.

The 3D medium is modeled as a half-space with Neumann boundary conditions only on the top surface. This is a typical geophysical geometry for the inverse problem. In this case the analytical solution, i.e. integral equation formulation, of the forward problem involves the mirror image of secondary sources. The analytical expression of sensitivity, in this case, can be described with a point-dipole source and its mirror image; hence, no modification of the cost function by subtracting the medium boundary effects is required in our 3D simulation.

4. Implementation and numerical results

In this section, we illustrate the anomaly reconstruction performance of the proposed projection-based level set approach through numerical simulations. We consider a 2D square medium of dimension 1 m × 1 m and a 3D medium with four boreholes, as shown in figure 4. The 2D medium is discretized in 1 cm × 1 cm grids and has 32 source electrodes, eight on each side of the boundary, that are shown as small black squares in the same figure. In our 2D ERT data we have 28 different experiments each with a distinct dipole source. The dipole sources are all chosen in a cross-medium configuration with eight horizontally, eight vertically and twelve diagonally oriented. In figure 4 the electrodes, for each source dipole, are connected with a dashed or a dotted line. The purpose behind such dipole configurations is to enforce electric current through the medium, and crossing anomalies, in different directions. We expect according to (5) that such a setup would lead to significant secondary sources on distinct portions of Γ and therefore producing data sets that are hopefully sensitive enough to the position and shape characteristics of Ω. In our simulations, we use the forward model described in [43], which is based on a resistor-network implementation. For the 2D medium, the model is modified to enforce Neumann boundary conditions on the whole boundary, whereas for 3D simulations the exact model as in [43] is used with Neumann boundary conditions on the top surface and mixed boundary conditions on the rest of the boundary.

In the first 2D set of simulations, we compare the performance of the projection-based approach to that of the gradient descent in reconstructing a conductivity anomaly having the shape of a half donut. The choice of such a shape is based on the fact that cavities are usually associated with low-sensitivity regions and therefore are difficult to reconstruct. The background and anomaly conductivity values are equal to 0.1 Sm^{-1} and 0.001 Sm^{-1}, respectively. For the projection-based approach we consider data sets with 1% and 5% additive Gaussian noise. The percentage values are computed with respect to the scattered potentials generated by the true anomaly. For the gradient-descent reconstructions, we also consider inversions using noise-free data. The same initial guess for the anomaly region Ω is used for both methods. In the implementation, the gradient-descent and projection-based speed
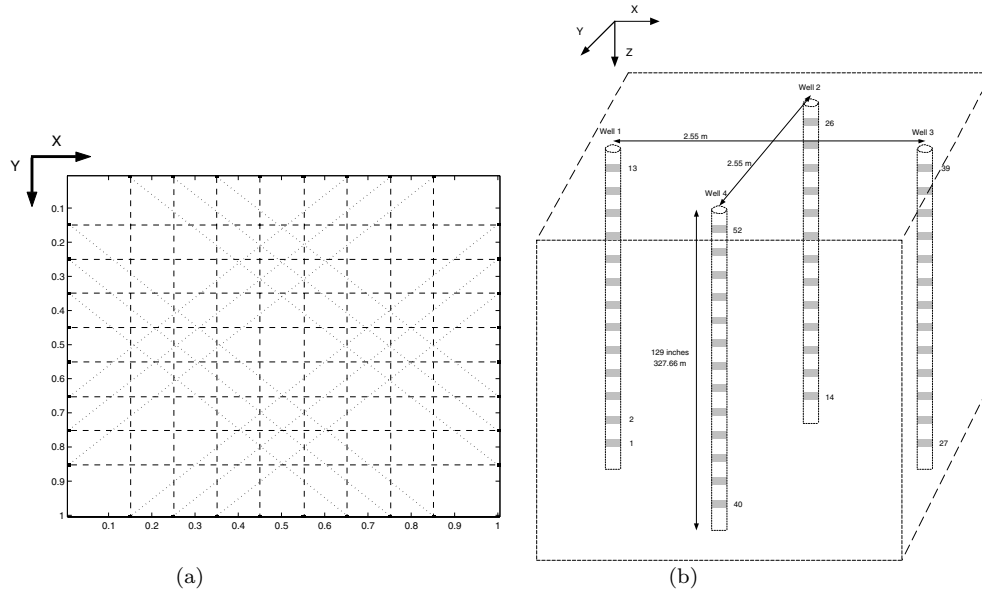
Figure 4. The media considered in this paper: (*a*) 2D medium with 32 source electrodes, i.e. eight on each boundary side (black squares), and 28 dipole-source configurations indicated in dashed-lines. (*b*) 3D medium, with four boreholes and 13 electrodes in each hole, represents a typical geophysical scenario.

functions are computed only within a thin narrow-band, i.e. at pixels defining the estimate anomalies' boundary, and the level-set function is re-initialized to a signed distance function every five iterations. The value of γ is chosen to be 0.01. This first estimate as well as the final reconstructions, from both methods, is displayed in figure 5. All results represent the estimates, in gray, at iteration 350. We also note that we use the same line search procedure, to identify the best time step in each iteration, for both methods. The obtained results show that the projection-based level set approach provides a more accurate reconstruction. In fact, the gradient-descent method seems to have some difficulties in pushing the front part of the contour to form a cavity. In figure 6 we plot three error measures, corresponding to reconstructions with the data set having 1% noise, illustrating the differences in performance between our approach and the gradient-descent level-set method. In figure 6(a) we plot the Log10 of averaged square residual errors (averaged by the number of iterations) for both reconstruction methods. In figures 6(b) and (c) we plot the errors describing the normalized intersection and mismatch areas between the actual anomaly Ω and its estimate Ω_{t_k} at time t_k corresponding to the kth iteration. The operator $\mathcal{A}$ is a measure of the area. The expression $\frac{\mathcal{A}(\Omega_{t_k} \bigcap \Omega)}{\mathcal{A}(\Omega)}$ represents the intersection area between Ω and Ω_{t_k} normalized by the area of the actual anomaly Ω. The second expression $\frac{\mathcal{A}(\Omega_{t_k} \setminus \Omega)}{\mathcal{A}(\Omega)}$ describes the false alarm area normalized by the area of Ω. In an accurate reconstruction the first expression should converge to 1, whereas the second one should converge to 0. The plots in figure 6 indicate that the projection-based level-set approach gives better reconstruction than the gradient-descent method with respect to the three error metrics. We also note that since we run both methods for only 350 iterations, the gradient-descent method, even if it converges, will require a lot more iterations than our proposed approach based on these results.
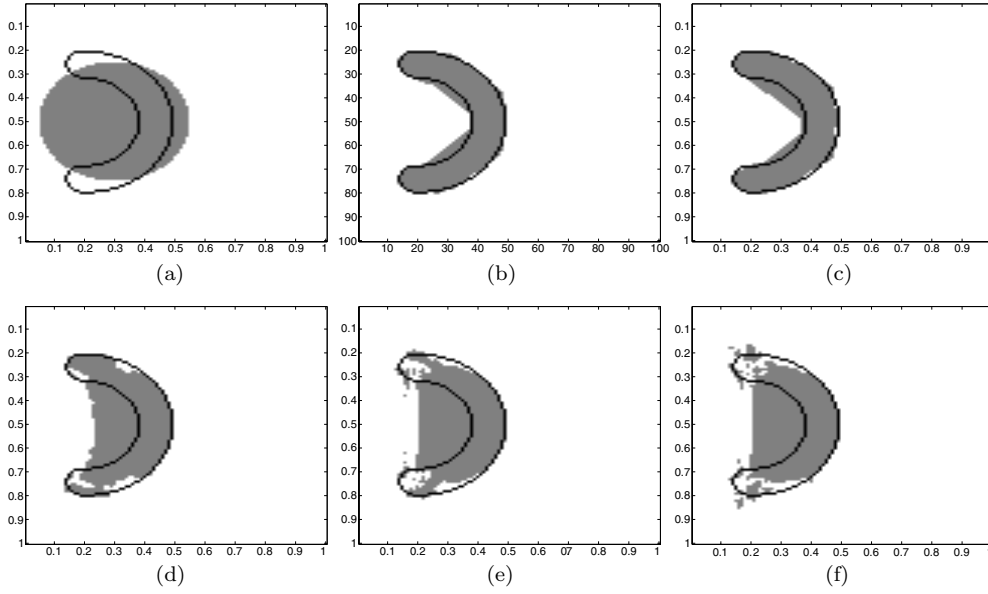
Figure 5. The reconstruction results for the projection-based approach and the gradient-descent method. In all sub-figures, the actual contour Γ is shown in black whereas the initial guess, for both methods (a) and the final estimates of Ω after 350 iterations (b)–(f) are shown in gray. The results indicate that the gradient-descent method has some difficulties to curve in the cavity whereas the projection-based approach shows very good reconstruction within the same number of iterations. (a) Initial guess and actual Γ, (b) projection-based method: final estimate with 1% noise, (c) projection-based method: final estimate with 5% noise, (d) gradient-descent method: final estimate with no noise, (e) gradient-descent method: final estimate with 1% noise and (f) gradient-descent method: final estimate with 5% noise.
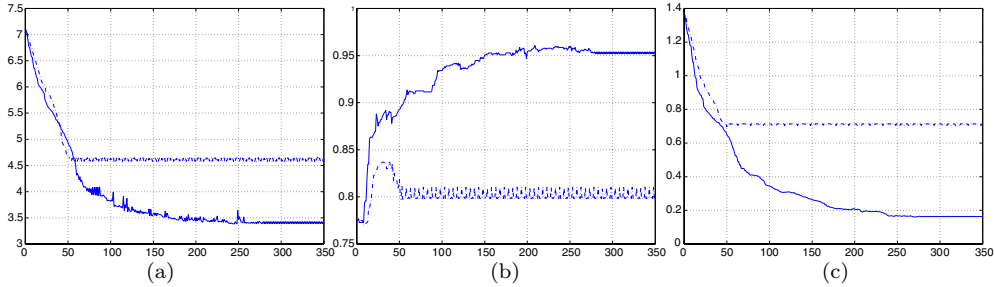
Figure 6. The residual error as well as the normalized mismatch errors between actual and estimated anomaly areas, for 1% data noise, at each kth iteration. Continuous lines show projection-based approach results whereas dashed lines correspond to gradient-descent method errors. (a) Log10 of residual errors versus iteration index k, (b) $\frac{\mathcal{A}(\Omega_{t_k} \cap \Omega)}{\mathcal{A}(\Omega)}$ versus k and (c) $\frac{\mathcal{A}(\Omega_{t_k} \setminus \Omega)}{\mathcal{A}(\Omega)}$ versus k.

In the second set of 2D simulations, the actual anomaly consists of three disjoint regions positioned far apart from each other. The initial guess, as shown in figure 7, does not provide any information or hint on the actual conductivity inhomogeneities. We make use of the same background and anomaly conductivity values as in the previous simulations and measured data with 1% additive noise. The speed functions are computed within a narrow band, as described
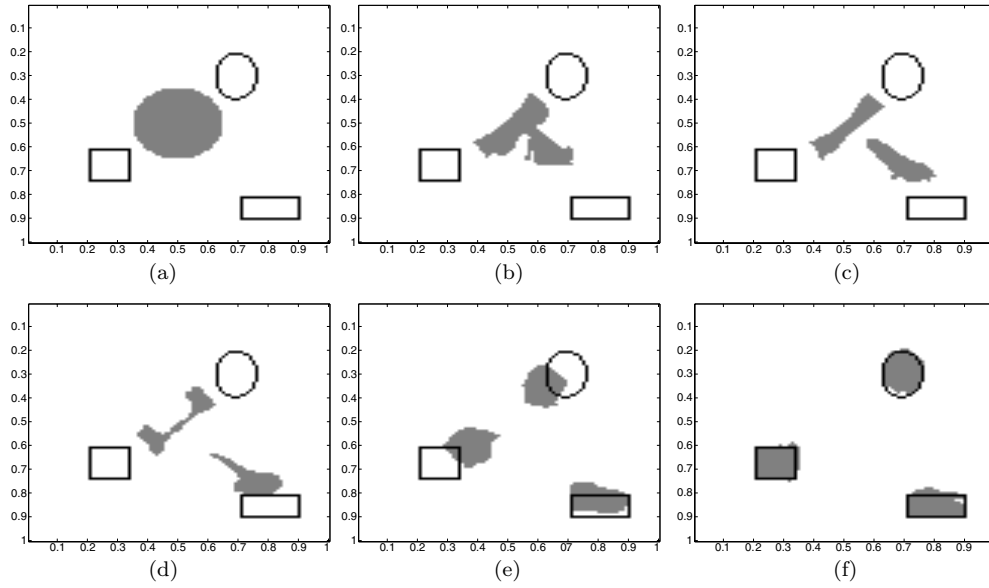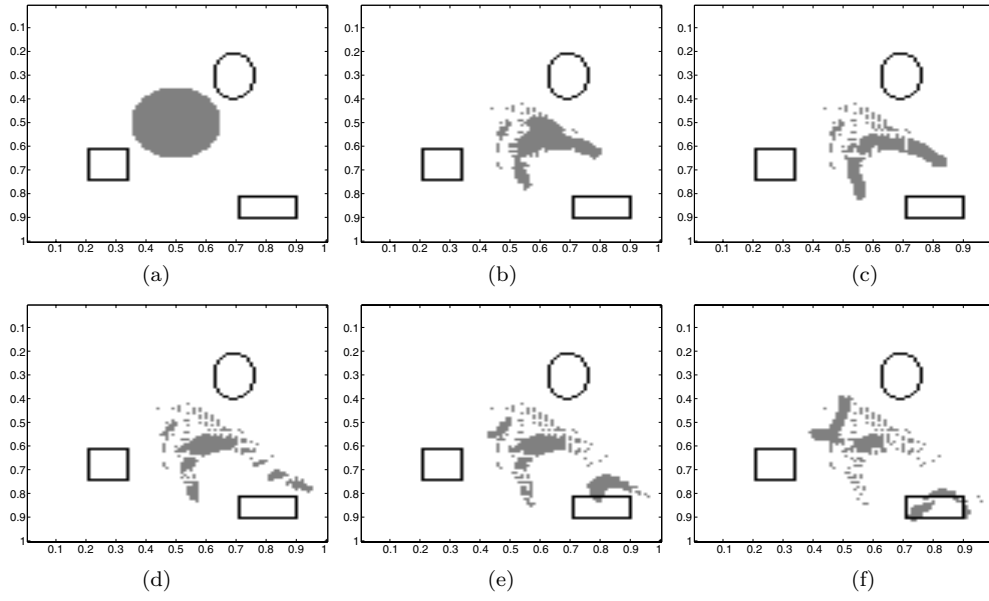
Figure 7. The evolution of the estimated Ω_t using projection-based level set reconstruction and measured data with 1% noise. The estimates of the anomalies are shown in gray whereas the actual Γ is shown in black in all sub-figures. The results clearly show a convergence in shape, position and number of anomalies of the estimate Ω_t to the actual inhomogeneity region. (a) Iteration 0, (b) iteration 50, (c) iteration 100, (d) iteration 200, (e) iteration 300 and (f) iteration 400.

above; the level-set functions are re-initialized every five iterations and $\gamma = 0.01$. Figure 7 illustrates the evolution of the projection-based reconstruction whereas figure 8 shows the estimates, based on the gradient-descent level-set method, at the same iterations. While our proposed approach converges to the actual anomalies, the gradient-descent velocity field seems to be driven mainly by the bottom-right rectangular anomaly which is closest to electrode sensors. After 400 iterations the gradient-descent estimate is clearly far from providing a reliable reconstruction of the three anomaly blobs. Figure 9 shows plots of residual errors as well as those of normalized mismatch metrics between estimated and actual regions for gradient-descent and projection-based level-set reconstruction. Our approach clearly indicates, in this simulation, a faster convergence to a better estimate of the actual anomaly regions.

The 3D simulation is intended to show the capability of the projection-based approach to converge even without much accuracy in choosing the time step τ_k in every kth iteration, e.g. without line search but rather a constant value for η. Such capability allows more computational efficiency especially when the number of unknowns, i.e. N, is very large. The 3D medium shown in figure 4 is discretized into $67 \times 67 \times 60$ voxels each with dimension 5.08 cm $\times$ 5.08 cm $\times$ 7.62 cm, i.e. 2 in $\times$ 2 in $\times$ 3 in. Conductivity values for background and anomalies are 0.05 Sm^{-1} and 0.0005 Sm^{-1}, respectively. Measured data sets correspond to 72 distinct dipole sources, i.e. 13×4 electrode pair combinations in horizontal cross-borehole configurations. A 5% Gaussian noise is added to the data. In the 3D simulation, only the projection-based level-set approach is tested. The speed function is computed only in the vicinity of the level zero, and the level set function, in this case, is re-initialized every iteration; however, no line search is applied for the time step. Instead the parameter η in equation (15) is chosen to be constant and equal to 0.65. Figure 10 shows the simulation results for two

Figure 8. The evolution of the estimated Ω_t using gradient-descent level-set reconstruction. The estimates of the anomalies at iterations 0, 50, 100, 200, 300 and 400 are shown in gray whereas the actual Γ is shown in black in all sub-figures. The results show a failure to converge to actual anomalies. As a matter of fact, it seems from the results that the gradient-descent level-set evolution is mainly driven by the bottom-right anomaly which is closest to sensor electrodes. (a) Iteration 0, (b) iteration 50, (c) iteration 100, (d) iteration 200, (e) iteration 300 and (f) iteration 400.
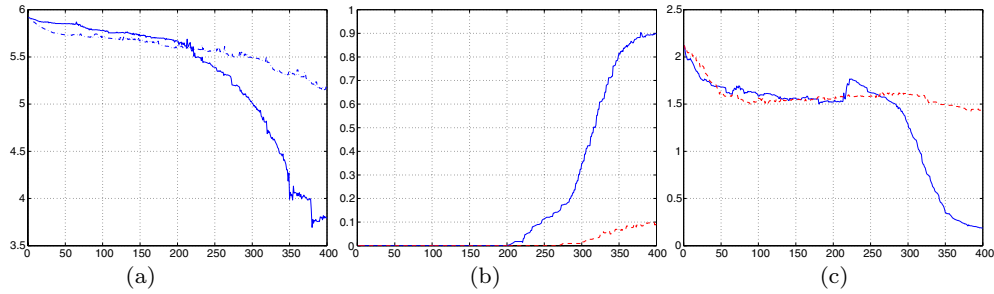
Figure 9. The residual error as well as the normalized mismatch errors between actual and estimated anomaly areas, for 1% data noise, at each kth iteration of the reconstruction of three disjoint anomalies. Continuous lines show projection-based approach results whereas break lines correspond to gradient-descent method errors. (a) Log10 of residual errors versus iteration index k, (b) $\frac{\mathcal{A}(\Omega_{t_k} \bigcap \Omega)}{\mathcal{A}(\Omega)}$ versus k and (c) $\frac{\mathcal{A}(\Omega_{t_k} \setminus \Omega)}{\mathcal{A}(\Omega)}$ versus k.

disjoint resistive blobs. Starting from an initial guess in the form of a sphere that does not intersect with actual anomalies (see figure 10) the projection-based level-set approach provides a reasonably accurate reconstruction of the actual conductivity inhomogeneity region Ω. The total number of iterations is 60, as shown in the residual error plot.
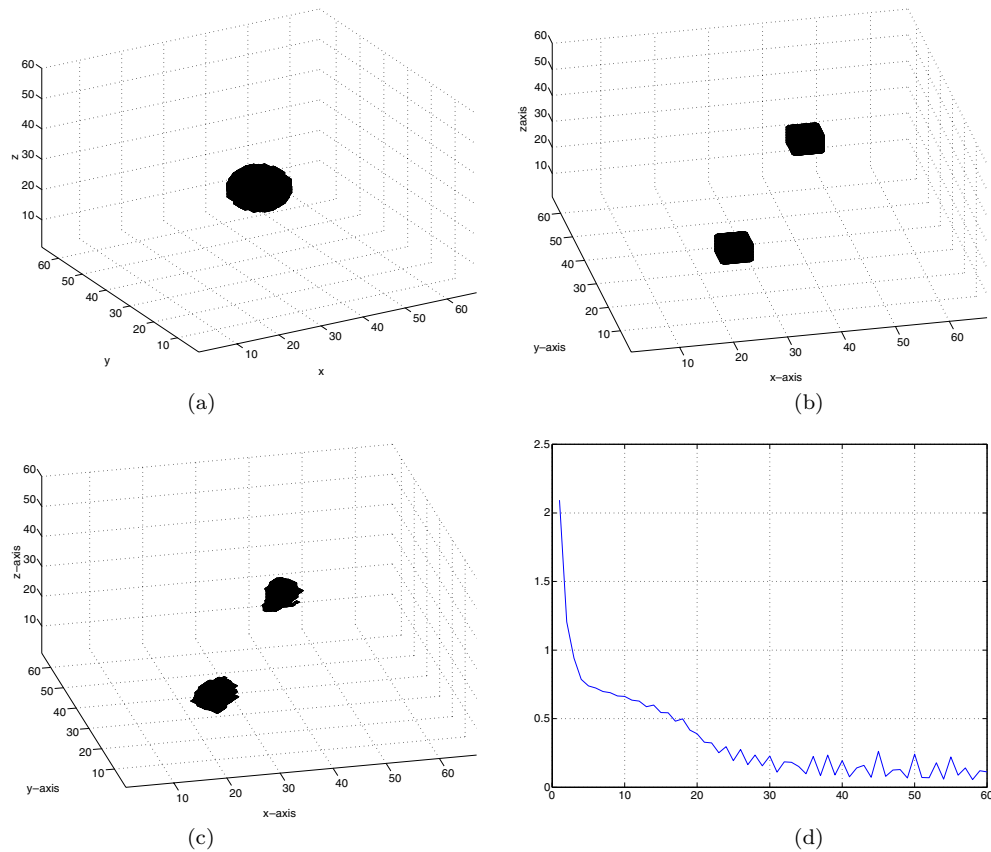
Figure 10. The initial guess, actual and reconstructed conductivity anomalies for a 3D simulation with two disjoint blobs as well as the residual error . The observation data has 5% additive Gaussian noise. Starting from a single spherical blob as initial guess, the proposed algorithm succeeds in locating both anomalies. (a) Initial guess, (b) actual anomalies, (c) reconstructed anomalies and (d) residual error.

5. Conclusion

In this paper we proposed a projection-based velocity field for level-set-based reconstruction of anomalies in low-sensitivity imaging modalities, specifically electrical resistance tomography. We showed that our approach is a descent method and we related its mathematical formulation to that of gradient-descent and Gauss–Newton-type methods. As described, the projection-based velocity field is shown, through numerical simulations, to overcome the effect of spatial variation of sensitivity on reconstruction performance. We also provided an efficient implementation of the proposed speed function that does not require any excessive forward or adjoint problem solves, as is the case for Gauss–Newton-type methods. In future work we consider investigating other alternatives of defining the speed function from distinct correlation coefficients, rather than using their sum, with more focus on 3D data. The formulation of the inverse problem as a reconstruction of secondary sources, using other level-set methods, will also be considered. Multi-source inversion can be carried in an unbounded medium which would require numerical evaluation of the accuracy of approximations estimating the effect

of the medium boundary on measured, or computed, electric potential. In the multi-source reconstruction approach, the localization of secondary sources would hopefully lead to a set of scattered points defining the boundary of conductivity anomalies.

Acknowledgments

Appendix A

The conductivity distribution $\sigma(r)$ described in (1) is not differentiable across Γ. In this section we consider weak differentiability by defining the standard mollifier, for each space dimension d,

$$\varphi_\epsilon(r) = \begin{cases} \dfrac{K_d}{\epsilon^d} \exp\left(\dfrac{\epsilon^2}{|r|^2 - \epsilon^2}\right) & \text{for} \quad |r| < \epsilon \\ 0 & \text{for} \quad |r| \geqslant \epsilon, \end{cases} \tag{A.1}$$

where ϵ is a small positive real number and K_d is chosen such that

$$\int_{\mathbb{R}^d} \varphi_\epsilon(r)\, dr = 1. \tag{A.2}$$

This family of functions is of class $C_0^\infty(\mathbb{R}^d)$. We then define the mollified conductivity σ_ϵ as

$$\sigma_\epsilon(r) = \int_{\mathbb{R}^d} \sigma(s)\varphi_\epsilon(r - s)\, ds \tag{A.3}$$

$$= \int_{\mathbf{B}_\epsilon(r)} \sigma(s)\frac{K_d}{\epsilon^d} \exp\left(\frac{\epsilon^2}{|r - s|^2 - \epsilon^2}\right) ds, \tag{A.4}$$

where $\mathbf{B}_\epsilon(r)$ is the d-dimensional sphere centered at r and with radius ϵ. According to (A.3), $\sigma_\epsilon \in C^\infty(\Omega)$ and $\sigma_\epsilon \longrightarrow \sigma$ as $\epsilon \longrightarrow 0$.
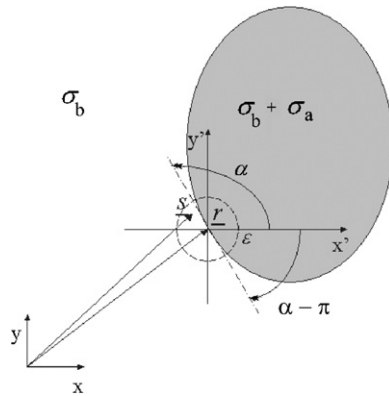
Given the differentiability of σ_ϵ, the corresponding forward problem can be described as

$$-\sigma_\epsilon \Delta u_\epsilon = \nabla u_\epsilon \cdot \nabla \sigma_\epsilon, \qquad \sigma_\epsilon \frac{\partial u_\epsilon}{\partial n} = f. \tag{A.5}$$

In the rest of this section we show that the limit of $\nabla \sigma_\epsilon$ as $\epsilon \longrightarrow 0$ is equal to $\sigma_a \nu$. Note that with such a result and by subtracting (4) from (A.5), in the limit where ϵ goes to 0, one gets the source-type formulation in (5). For simplicity, we consider only the 2D case, the derivations for a 3D medium are similar.

Let $r = [x_r\, y_r]^T$ be a point in $\mathcal{D}$ and $B_\epsilon(r)$ be the disc with center r and radius ϵ, where ϵ is a small positive real number. Let $s = [x_s\, y_s]^T$ be a point in the same disc (see figure A1). Considering equation (A.4), with $d = 2$, the derivatives of σ_ϵ in the x- and y-directions can be expressed as

$$\frac{\partial \sigma_\epsilon}{\partial x_r} = \int_{\mathbf{B}_\epsilon(r)} \frac{K_2}{\epsilon^2} \sigma(s) \frac{-2(x_r - x_s)\epsilon^2}{(\|r - s\|^2 - \epsilon^2)^2} \exp\left(\frac{\epsilon^2}{\|r - s\|^2 - \epsilon^2}\right) ds \tag{A.6}$$

Figure A1. An illustration of the picture behind the derivations in appendix A.

and

$$\frac{\partial \sigma_\epsilon}{\partial y_r} = \int_{\mathbf{B}_\epsilon(r)} \frac{K_2}{\epsilon^2} \sigma(s) \frac{-2(y_r - y_s)\epsilon^2}{(\|r - s\|^2 - \epsilon^2)^2} \exp\left(\frac{\epsilon^2}{\|r - s\|^2 - \epsilon^2}\right) ds. \tag{A.7}$$

In a polar coordinate system, with origin at r, $x_s - x_r = R \cos\theta$ and $y_s - y_r = R \sin\theta$ where R is the distance between the points r and s and θ the angle between the x-axis and $s - r$. Equations (A.6) and (A.7) can then be written as

$$\nabla \sigma_\epsilon(r) = \frac{K_2}{\epsilon^2} \begin{bmatrix} \int_0^\epsilon \int_{-\pi}^\pi \frac{2\epsilon^2 R \cos\theta}{(R^2-\epsilon^2)^2} \exp\left(\frac{\epsilon^2}{R^2-\epsilon^2}\right) \sigma(R,\theta) R \, d\theta \, dR \\ \int_0^\epsilon \int_{-\pi}^\pi \frac{-2\epsilon^2 R \sin\theta}{(R^2-\epsilon^2)^2} \exp\left(\frac{\epsilon^2}{R^2-\epsilon^2}\right) \sigma(R,\theta) R \, d\theta \, dR \end{bmatrix} \tag{A.8}$$

$$= \frac{K_2}{\epsilon^2} \int_0^\epsilon h_\epsilon(R) \left(\int_{-\pi}^\pi \sigma(R,\theta) \begin{bmatrix} \cos\theta \\ \sin\theta \end{bmatrix} d\theta \right) dR, \tag{A.9}$$

where

$$h_\epsilon(R) = \frac{2\epsilon^2 R^2}{(R^2 - \epsilon^2)^2} \exp\left(\frac{\epsilon^2}{R^2 - \epsilon^2}\right). \tag{A.10}$$

In the case where $r \notin \Gamma$, there exists an ϵ smaller than the distance between r and Γ. In such a case $\sigma(R, \theta)$ is constant inside $B_\epsilon(r)$, i.e. equal to σ_b or $\sigma_b + \sigma_a$, and hence independent of θ which implies $\nabla \sigma_\epsilon = 0$ since the integrals of $\cos\theta$ and $\sin\theta$ over the interval $[-\pi, \pi]$ are both equal to 0. However, if $r \in \Gamma$ then $\sigma(R, \theta)$ is either equal to σ_b or $\sigma_b + \sigma_a$ depending on whether $s \in \mathcal{D} \backslash \Omega$ or $s \in \Omega$. For small ϵ, we can approximate the regions $B_\epsilon(r) \cap (\mathcal{D} \backslash \Omega)$ and $B_\epsilon(r) \cap \Omega$ by the half discs separated by the tangent to Γ at point r, as shown in figure A1. Let α be the angle between the x-axis and the same tangent and define the integral I_α as

$$I_\alpha = \int_{\alpha-\pi}^\alpha (\sigma_b + \sigma_a) \begin{bmatrix} \cos\theta \\ \sin\theta \end{bmatrix} d\theta + \int_\alpha^{\alpha+\pi} \sigma_b \begin{bmatrix} \cos\theta \\ \sin\theta \end{bmatrix} d\theta \tag{A.11}$$

$$= \sigma_a \begin{bmatrix} -2\sin\alpha \\ 2\cos\alpha \end{bmatrix}. \tag{A.12}$$

The gradient of σ_ϵ can then be described as

$$\nabla \sigma_\epsilon = \sigma_a \begin{bmatrix} -\sin \alpha \\ \cos \alpha \end{bmatrix} \int_0^\epsilon \frac{2K_2}{\epsilon^2} h_\epsilon(R) \, \mathrm{d}R. \tag{A.13}$$

Let us call the integral in (A.13) I_ϵ; then using integration by parts we have

$$I_\epsilon = -\frac{2K_2}{\epsilon^2} \left[R \exp \left(\frac{\epsilon^2}{R^2 - \epsilon^2} \right) \right]_0^\epsilon + \frac{K_2}{\epsilon} \int_0^\epsilon \frac{2}{\epsilon} \exp \left(\frac{\epsilon^2}{R^2 - \epsilon^2} \right) \mathrm{d}R \tag{A.14}$$

$$= 0 + \frac{K_2}{K_1 \epsilon} \int_{-\epsilon}^\epsilon \frac{K_1}{\epsilon} \exp \left(\frac{\epsilon^2}{R^2 - \epsilon^2} \right) \mathrm{d}R. \tag{A.15}$$

The integrand in (A.15) is the standard 1D mollifier and K_1 is chosen so that the integral is equal to 1. Thus $I_\epsilon = \frac{K_2}{K_1 \epsilon}$ and by substituting its value in (A.13) we can write $\nabla \sigma_\epsilon$ as

$$\nabla \sigma_\epsilon = \frac{K_2}{K_1 \epsilon} \sigma_a \nu \tag{A.16}$$

for $r \in \Gamma$. Note that the outward unit normal of Γ is equal to $[-\sin \alpha \cos \alpha]^T$ and numerically $K_1 \cong K_2$. Considering both cases, i.e. whether $r \in \Gamma$ or not,

$$\nabla \sigma = \lim_{\epsilon \to 0} \nabla \sigma_\epsilon \tag{A.17}$$

$$= \sigma_a \nu \delta_\Gamma \tag{A.18}$$

where δ_Γ is the Dirac delta function with non-zero support equal to Γ. This concludes our proof. For a 3D medium, the derivations would be the same, except that $B_\epsilon(r)$ will be a sphere and we have to use a spherical coordinate system, instead of polar, to evaluate the corresponding integrals.

Appendix B

In this section, we derive the link between the variational (19) and adjoint (27) formulations of the speed function by showing that $(u'_{l,r}, u_l - z_l)_{\partial \mathcal{D}} = \nabla u_l(r) \cdot \nabla w_l(r)$. Let $\delta \sigma$ be the conductivity perturbation at location r associated with the change $u'_{l,r}$ in the potential function u_l. The forward problem for the perturbed conductivity can then be described as

$$\nabla \cdot ((\sigma + \delta \sigma) \nabla (u_l + u'_{l,r})) = 0, \qquad (\sigma + \delta \sigma) \frac{\partial (u_l + u'_{l,r})}{\partial n} = f. \tag{B.1}$$

Subtracting (2) from (B.1) and ignoring the second-order terms, $u'_{l,r}$ is found to be the solution of the boundary value problem

$$\nabla \cdot (\sigma \nabla u'_{l,r}) = -\nabla \cdot (\delta \sigma \nabla u_l), \qquad \sigma \frac{\partial u'_{l,r}}{\partial n} = -\delta \sigma \frac{\partial u_l}{\partial n}. \tag{B.2}$$

Note that one needs to solve (B.2) for each sensitivity function associated with u_l and a location r.

In the adjoint problem description (26) the residual error is equal to $\sigma \frac{\partial w_l}{\partial n}$. Therefore using Green's first identity the dot product $(u'_{l,r}, u_l - z_l)_{\partial D}$ is equal to

$$(u'_{l,r}, u_l - z_l)_{\partial \mathcal{D}} = \int_{\mathcal{D}} u'_{l,r} \nabla \cdot (\sigma \nabla w_l) + \int_{\mathcal{D}} \sigma \nabla u'_{l,r} \cdot \nabla w_l \tag{B.3}$$

$$= \int_{\mathcal{D}} \sigma \nabla u'_{l,r} \cdot \nabla w_l. \tag{B.4}$$

The first integral in (B.3) is equal to 0 because $\nabla \cdot (\sigma \nabla w_l) = 0$ according to (26). In the next step, we apply Green's first identity to (B.4) using $\sigma \nabla u'_{l,r}$ as the vector field of interest. The result is

$$(u'_{l,r}, u_l - z_l)_{\partial \mathcal{D}} = \oint_{\partial \mathcal{D}} w_l \sigma \frac{\partial u'_{l,r}}{\partial n} \mathrm{d}s - \int_{\mathcal{D}} w_l \nabla \cdot (\sigma \nabla u'_{l,r}) \qquad (\text{B.5})$$

$$= -\oint_{\partial \mathcal{D}} w_l \delta \sigma \frac{\partial u_l}{\partial n} \mathrm{d}s + \int_{\mathcal{D}} w_l \nabla \cdot (\delta \sigma \nabla u_l) \qquad (\text{B.6})$$

where (B.6) is obtained from (B.5) by substituting $-\delta\sigma \frac{\partial u_l}{\partial n}$ for $\sigma \frac{\partial u'_{l,r}}{\partial n}$ and $-\nabla \cdot (\delta\sigma \nabla u_l)$ for $\nabla \cdot (\sigma \nabla u'_{l,r})$ based on the boundary value problem (B.2). Applying Green's first identity, once more, to the contour integral in (B.6) implies

$$\oint_{\partial \mathcal{D}} w_l \delta\sigma \frac{\partial u_l}{\partial n} \mathrm{d}s = \int_{\mathcal{D}} w_l \nabla \cdot (\delta\sigma \nabla u_l) + \int_{\mathcal{D}} \delta\sigma \nabla w_l \cdot \nabla u_l. \qquad (\text{B.7})$$

Finally by substituting (B.7) in (B.6) we end up with

$$(u'_{l,r}, u_l - z_l)_{\partial \mathcal{D}} = -\int_{\mathcal{D}} \delta\sigma(q) \nabla w_l \cdot \nabla u_l \, \mathrm{d}(q). \qquad (\text{B.8})$$

In the case where $\delta\sigma$ is equal to the dirac delta function at the point r, the sensitivity functions can be related to the adjoint potential as $(u'_{l,r}, u_l - z_l)_{\partial \mathcal{D}} = \nabla u_l(r) \cdot \nabla w_l(r)$. The use of the dirac delta function for the conductivity perturbation is possible in the weak differentiability sense.

Appendix C

Let t be a time instance and δt a very small time interval. We define $\Gamma_{t+\delta t}$ as a slightly deformed version of Γ_t:

$$\Gamma_{t+\delta t} = \{q; q = q' + v(q', t)\delta t \nu \text{ where } q' \in \Gamma_t\}, \qquad (\text{C.1})$$

where $v(q', t)$ is a scalar velocity function and ν is the outward unit normal of Γ_t. In an unbounded medium, the difference in scattered potentials corresponding to $\Gamma_{t+\delta t}$ and Γ_t can be described, according to (7) and (35), as

$$\widetilde{u}_{s,l}^{t+\delta t}(r) - \widetilde{u}_{s,l}^t(r) = \rho_b \oint_{\Gamma_{t+\delta t}} c_l(q, t + \delta t) g(q, r) \, \mathrm{d}s - \rho_b \oint_{\Gamma_t} c_l(q, t) g(q, r) \, \mathrm{d}s, \qquad (\text{C.2})$$

where l here represents experiment, or data set, index and c_l describes the equivalent secondary sources corresponding to the anomaly. Using the definition in (C.1) and assuming that δt is very small, equation (C.2) can be re-written as

$$\widetilde{u}_{s,l}^{t+\delta t}(r) - \widetilde{u}_{s,l}^t(r) = -\rho_b \oint_{\Gamma_t} c_l(q', t) g(q', r) \, \mathrm{d}s$$

$$+ \rho_b \oint_{\Gamma_t} c_l(q' + v(q', t)\nu\delta t, t) g(q' + v(q', t)\nu\delta t, r) \, \mathrm{d}s. \qquad (\text{C.3})$$

Let $\zeta(q', r, t, \delta t)$ be the integrand of the second integral in (C.3). By applying a first-order linear approximation ζ can be expressed as

$$\zeta = (c_l(q', t) + \dot{c}_l(q', t)v(q', t)\delta t) \left(g(q', t) + \frac{\partial g}{\partial \nu} v(q', t)\delta t \right), \qquad (\text{C.4})$$

where $\dot{c}_l$ represent the variation in the amplitudes of the equivalent secondary sources due to the contour deformation and $\frac{\partial g}{\partial \nu}$ is derivative of the Green function in the normal direction ν of Γ_t.

In order to evaluate sensitivity, analytically, we consider a localized contour deformation. In other words assume that $v(q, t)$ is non-zero only within a very small neighborhood of a point $p \in \Gamma_t$. In such a case the change in the equivalent sources' amplitudes is negligible given the small change in total potential (see the expression of secondary sources in (5)). Under this assumption, we substitute (C.4) in (C.3) with $\dot{c}_l(q', t) = 0$, which leads to

$$
\begin{aligned}
\widetilde{u}_{s,l}^{t+\delta t}(r) - \widetilde{u}_{s,l}^{t}(r) \cong & -\rho_b \oint_{\Gamma_t} c_l(q', t) g(q', r) \, \mathrm{d}s \\
& + \rho_b \oint_{\Gamma_t} c_l(q', t) g(q', r) \, \mathrm{d}s \\
& + \oint_{\Gamma_t} c_l(q', t) \frac{\partial g(q', r)}{\partial \nu} \alpha(q', t) \delta t \, \mathrm{d}s \\
= & \oint_{\Gamma_t} c_l(q', t) \frac{\partial g(q', r)}{\partial \nu} \delta q' \, \mathrm{d}s.
\end{aligned}
\tag{C.5}
$$

The term $\delta q' = v(q', t)\delta t$ describes the displacement of the contour and is non-zero only within a small arc centered at p. As the contour displacement becomes restricted to a point $p \in \Gamma_t$, i.e. $\delta q' = v$ at point p and 0 elsewhere, the sensitivity of the scattered potential to such localized displacement is

$$
u'_{l,p}(r) = c_l(p, t) \nabla g(p, r) \cdot v.
\tag{C.6}
$$

This formulation implies that sensitivity in this case is linearly proportional to the potential function produced by a point dipole source located on Γ_t and in the same direction as ν. In our approach, and since we are interested in the correlation coefficient between sensitivity function and residual error, we can ignore the multiplicative term $c_l(p, t)$ and just use $\nabla g(p, r) \cdot v$ for sensitivity functions. This is not an approximation and it does not affect the resulting projection-based speed function because amplitudes of both sensitivity and residual error get washed out in computing the correlation coefficients.

References

[1] Bell F G 2004 *Engineering Geology and Construction* 1st edn (London: Spon)
[2] Holder D 1993 *Clinical and Physiological Applications of Electrical Impedance Tomography* 1st edn (London: UCL Press)
[3] Harris N D, Suggett A J, Barber D and Brown B 1987 Applications of applied potential tomography (APT) in respiratory medicine *Clin. Phys. Physiol. Meas.* **8** 155–65
[4] Cheney M, Isaacson D and Newell J C 1999 Electrical impedance tomography *SIAM Rev.* **41** 85–101
[5] Frerichs I, Hahn G and Hellige G 1999 Thoracic electrical impedance tomographic measurements during volume controlled ventilation-effects of tidal volume and positive end-expiratory pressure *IEEE Trans. Med. Imaging* **18** 764–73
[6] Chrepenin V A, Karpov A Y, Korjenevsky A V, Kornienko V N, Kultiasov Y S, Ochapkin M B, Trochanova O V and Meister J D 2002 Three-dimensional EIT imaging of breast tissues: system design and clinical testing *IEEE Trans. Med. Imaging* **21** 662–7
[7] Frerichs I, Hinz J, Herrmann P, Weisser G, Hahn G, Quintel M and Hellige G 2002 Regional lung perfusion as determined by electrical impedance tomography in comparison with electron beam CT imaging *IEEE Trans. Med. Imaging* **21** 646–52
[8] Gonçalves S I, de Munck J C, Verbunt J P A, Bijma F, Heethaar R M and da Silva F L 2003 In vivo measurement of the brain and skull resistivities using and EIT-based method and realistic models for the head *IEEE Trans. Biomed. Eng.* **50** 754–67

 [9] Choi M H, Kao T J, Isaacson D, Saulnier G J and Newell J C 2007 A reconstruction algorithm for breast cancer imaging with electrical impedance tomography in mammography geometry *IEEE Trans. Biomed. Eng.* **54** 700–10

[10] Alessandrini G and Rondi L 1998 Stable determination of a crack in a planar inhomogeneous conductor *SIAM J. Math. Anal.* **30** 326–40

[11] Santosa F and Vogelius M S 1991 A computational algorithm to determine cracks from electrostatic boundary measurements *Int. J. Eng. Sci.* **29** 917–38

[12] Santosa F, Kaup P and Vogelius M S 1996 A method for imaging corrosion damage in thin plates from electrostatic data *Inverse Problems* **12** 279–93

[13] Cedio-Fengya D J, Moskow S and Vogelius M S 1998 Identification of conductivity imperfections of small diameter by boundary measurements continuous dependence and computational reconstruction *Inverse Problems* **14** 553–95

[14] Dines K and Lytle R 1981 Analysis of electrical conductivity imaging *Geophysics* **46** 1025–36

[15] Parker R L 1984 The problem of resistivity sounding *Geophysics* **142** 2143–58

[16] Ramirez A, Daily W, Binley B, LaBrecque D J and Roelant D 1996 Detection of leaks in underground storage tanks using electrical resistance methods *J. Environ. Eng. Geophys.* **1** 189–203

[17] Yuval and Oldenburg D W 1996 DC resistivity and IP methods in acid mine drainage problems: results from the Copper Cliff mine tailings impoundments *J. Appl. Geophys.* **34** 187–98

[18] Daily W and Ramirez A L 2000 Electrical imaging of engineered hydraulic barriers *Geophysics* **65** 83–94

[19] Pidlisecky A, Knight R and Haber E 2006 Cone-based electrical resistivity tomography *Geophysics* **71** G157–G167

[20] Caldéron A P 1980 On an inverse boundary value problem *Seminar on Numerical Analysis and its Applications to Continuum Physics, Soc. Brasiliera de Matemàtica* pp 65–73

[21] Kohn R V and Vogelius M 1984 Determining conductivity by boundary measurements *Commun. Pure Appl. Math.* **37** 289–98

[22] Kohn R V and Vogelius M 1985 Determining conductivity by boundary measurements: II. Interior results *Commun. Pure Appl. Math.* **38** 643–67

[23] Sylvester J and Uhlmann G 1987 A global uniqueness theorem for an inverse boundary value problem *Ann. Math. (2)* **125** 153–69

[24] Nachmann A I, Sylvester J and Uhlmann G 1988 An *n*-dimensional Borg–Levinson theorem *Commun. Math. Phys.* **115** 595–605

[25] Borcea L 2002 Electrical impedance tomography *Inverse Problems* **18** R99–R136

[26] Brown B H 2003 Electrical impedance tomography (EIT): A review *J. Med. Eng. Technol.* **3** 97–108

[27] Lionheart W R 2004 EIT reconstruction algorithms: pitfalls, challenges and recent developments *Physiol. Meas.* **1** 125–42

[28] Barber D C and Brown B H 1986 Recent developments in applied potential tomography-apt *Information Processing in Medical Imaging* ed S L Bacharach (Amsterdam: Nijhoff) pp 106–21

[29] Santosa F and Vogelius M S 1990 A backprojection algorithm for electrical impedance imaging *SIAM J. Appl. Math.* **50** 216–43

[30] Frangi A F, Riu P J, Rosell J and Viergever M A 2002 Propagation of measurement noise through backprojection reconstruction in electrical impedance tomography *IEEE Trans. Med. Imaging* **21** 566–78

[31] Cheney M, Isaacson D, Newell J C, Simske S and Goble J C 1990 NOSER: an algorithm for solving the inverse conductivity problem *Int. J. Imaging Syst. Technol.* **2** 66–75

[32] Le Hyaric A and Pidcock m K 2001 An image reconstruction algorithm for three-dimensional electrical impedance tomography *IEEE Trans. Biomed. Eng.* **48** 230–5

[33] Curtis E B and Morrow J A 1990 Determining the resistors in a network *SIAM J. Appl. Math.* **50** 931–41

[34] Somersalo E, Cheney M, Isaacson D and Isaacson E 1991 Layer stripping: a direct numerical method for impedance imaging *Inverse Problems* **7** 899–926

[35] Sylvester J 1992 A convergent layer stripping algorithm for radially symmetric impedance tomography problem *Commun. Partial Diff. Eqns* **17** 1955–94

[36] Siltanen S, Mueller J and Isaacson D 2000 An implementation of the reconstruction algorithm of A Nachman for the 2D inverse conductivity problem *Inverse Problems* **16** 681–99

[37] Mueller J and Siltanen S 2003 Direct reconstructions of conductivities from boundary measurements *SIAM J. Sci. Comput.* **24** 1232–66

[38] Brühl M 2001 Explicit characterization of inclusions in electrical impedance tomography *SIAM J. Math. Anal.* **32** 1327–41

[39] Hanke M and Brühl M 2003 Recent progress in electrical impedance tomography *Inverse Problems* **16** 651–63

[40] Oldenburg D W, McGillivray P R and Ellis R G 1993 Generalized subspace methods for large-scale inverse problems *Geophys. J. Int.* **114** 12–20

[41] Oldenburg D W and Yaoguo Li 1994 Subspace linear inverse method *Inverse Problems* **10** 915–35

[42] Ellis R G and Oldenburg D W 1994 Applied geophysics inversion *Geophysics J. Int.* **116** 5–11

[43] Zhang J, Mackie R L and Madden T R 1995 3-D resistivity forward modeling and inversion using conjugate gradients *Geophysics* **60** 1313–25

[44] LaBrecque D J, Morelli G, Daily W, Ramirez A and Lundegard P 1999 Occam's inversion of 3D ERT data *Three-Dimensional Electromagnetics, SEG* ed B Spies (Tulsa, OK) pp 575–90

[45] Ellis R G and Oldenburg D W 1994 3-D DC-resistivity inverse problem: a conjugate gradient approach *Geophys. J. Int.* **119** 187–95

[46] Haber E, Ascher U M and Oldenburg D W 2000 On optimization techniques for solving nonlinear inverse problems *Inverse Problems* **16** 1263–80

[47] Haber E and Ascher 2001 U M Preconditioned all-at-one methods for large, sparse parameter estimation problems *Inverse Problems* **17** 1847–64

[48] Newmann G A and Boggs P T 2004 Solution accelerators for large-scale three-dimensional electromagnetic inverse problems *Inverse Problems* **20** S151–S170

[49] Haber E 2005 Quasi-Newton methods for large-scale electromagnetic inverse problems *Inverse Problems* **21** 305–23

[50] Lechleiter A and Rieder A 2006 Newton regularizations for impedance tomography: a numerical study *Inverse Problems* **22** 1967–87

[51] Ascher U M, Haber E and Huang H 2006 On effective methods for implicit piecewise smooth surface recovery *SIAM J. Sci. Comput.* **28** 339–58

[52] Haber E and Tenorio L 2003 Learning regularization functionals–a supervised training approach *Inverse Problems* **19** 611–26

[53] Borcea L, Gray G A and Zhang Y 2003 Variationally constrained numerical solution of electrical impedance tomography *Inverse Problems* **19** 1159–84

[54] Vauhkonen M, Kaipio J P, Somersalo E and Karjalainen P A 1997 Electrical impedance tomography with basis constraints *Inverse Problems* **13** 523–30

[55] Kaipio J P, Kolehmainen, Somersalo E and Vauhkonen M 2000 Statistical inversion and Monte Carlo sampling methods in electrical impedance tomography *Inverse Problems* **16** 1487–522

[56] Yang X 1999 Stochastic inversion of 3-D ERT data *PhD Thesis* University of Arizona

[57] Chou K C and Willsky A S 1989 A multi-resolution, probabilistic approach to two dimensional inverse conductivity problem *Signal Process.* **18** 291–311

[58] Borcea L 2001 A nonlinear multigrid for imaging electrical conductivity and permittivity at low frequency *Inverse Problems* **17** 329–58

[59] Ascher U M and Haber E 2001 Grid refinement and scaling for distributed parameter estimation problems *Inverse Problems* **17** 571–90

[60] Santosa F 1996 A level set approach for inverse problems involving obstacles *ESAIM: Control, Optimisation Calculus Variations* **1** 17–33

[61] Harabetian E and Osher S 1998 Regularization of ill-posed problems via the level set approach *SIAM J. Appl. Math.* **58** 1689–1706

[62] Litman A, Lesselier D and Santosa F 1998 Reconstruction of a two-dimensional binary obstacle by controlled evolution of a level-set *Inverse Problems* **14** 685–706

[63] Dorn O, Miller E L and Rappaport C M 2000 A shape reconstruction method for electromagnetic tomography using adjoint fields and level sets *Inverse Problems* **16** 1119–56

[64] Ito K, Kunisch K and Li Z 2001 Level-set function approach to an inverse interface problem *Inverse Problems* **17** 1225–42

[65] Burger M 2001 A level set method for inverse problems *Inverse Problems* **17** 1327–55

[66] Chan T F and Tai X C 2003 Level set and total variational regularization for elliptic inverse problems with discontinuous coefficients *J. Comput. Phys.* **193** 40–66

[67] Chung E T, Chan T F and Tai X C 2005 Electrical impedance tomography using level set representation and total variational regularization *J. Comput. Phys.* **205** 357–72

[68] Ben Hadj Miled M K and Miller E L 2001 On the extension of level-set curve evolution methods for low-sensitivity imaging problems *ICIP Proc.* **II** 625–8

[69] Soleimani M, Lionheart W R B and Dorn O 2006 Level set reconstruction of conductivity and permittivity from boundary electrical measurements using experimental data *Inverse Problems Sci. Eng.* **14** 193–210

[70] Soleimani M, Dorn O and Lionheart W R B 2006 A narrow-band level set method applied to EIT in brain for cryosurgery monitoring *IEEE Trans. Biomed. Eng.* **53** 2257–64

[71] Berger M 2004 Levenberg–Marquardt level set methods for inverse problems *Inverse Problems* **20** 259–82
[72] van den Doel K and Ascher U M 2006 On level set regularization for highly ill-posed distributed parameter estimation problems *J. Comput. Phys.* **216** 707–23
[73] Dorn O and Lesselier D 2006 Level set methods for inverse problems *Inverse Problems* **22** R67–131
[74] Osher S and Sethian J 1988 Fronts propagation with curvature dependent speed: algorithms based on Hamilton–Jacobi formulations *J. Comput. Phys.* **56** 12–49
[75] Ben Ameur H, Burger M and Hackl B 2004 Level set methods for geometric inverse problems in linear elasticity *Inverse Problems* **20** 673–96
[76] Sethian J A 1999 *Level Set Methods and Fast Marching Methods* 2nd edn (Cambridge: Cambridge University Press)